Frontiers of Information Technology & Electronic Engineering
www.jzus.zju.edu.cn; engineering.cae.cn; www.springerlink.com
ISSN 2095-9184 (print); ISSN 2095-9230 (online)
E-mail: jzus@zju.edu.cn

Multiplication extended kalman filter-aided non-blind star image restoration algorithm based on the heterogeneous blur kernel

Yang LIU[1,2,3], Huajian DENG[1], Hao WANG[‡1,2,3], Zhonghe JIN[1,2,3]

[1]*Micro-Satellite Research Center, Zhejiang University, Hangzhou 310027, China*

[2]*Huanjiang Laboratory, Zhuji 311800, China*

[3]*Key Laboratory of Micro-Nano Satellite Research Zhejiang Province, Hangzhou 310027, China*

E-mail: 12224002@zju.edu.cn; denghuajian@zju.edu.cn; roger@zju.edu.cn; jinzh@zju.edu.cn

Received Mar. 29, 2025; Revision accepted June 10, 2025; Crosschecked

Abstract: Under dynamic conditions, the smearing effect of star spots on the image plane reduces centroid extraction accuracy, which has an impact on attitude estimation. To enhance the dynamic performance of the star sensor, we propose a multiplication extended Kalman filter (MEKF)-aided non-blind star image restoration algorithm based on the heterogeneous blur kernel. The proposed algorithm consists of three procedures. First, the MEKF is used to estimate the attitude and gyro drift to eliminate the measurement error of the star sensor and gyro drift. Second, the attitude predicted by MEKF is used, which provides initial conditions and accelerates the subsequent algorithm. Finally, gyro assisted heterogeneous blur kernel estimation algorithm is presented for restoring non-uniform and nonlinear motion-blurred star images. In contrast to existing dynamic star image deblurring algorithms, which focus mostly on image content, the proposed method emphasizes the cause of motion blur fusing MEKF and a heterogeneous blur kernel. This leads to significantly enhanced robustness against noise and improved restoration accuracy. Simulation results demonstrate that the proposed method significantly outperforms existing techniques, improving centroid extraction accuracy by up to 59.64% and pointing accuracy across all axes by more than 78%.

Unedited

Key words: Heterogeneous blur kernel estimation; Dynamic conditions; Regional image restoration; Multiplication extended Kalman filter; Gyro drift

https://doi.org/10.1631/FITEE.2500193 **CLC number:**

1 Introduction

With the advancement of the space industry, there is an increasing demand for attitude measurement, especially under dynamic conditions. The star sensor is one of the most common and important attitude measurement devices, providing high-precision attitude measurement under static conditions. However, under dynamic conditions, star spots will form trails on the image plane. The signal-to-noise ratio (SNR) of star spots will significantly decrease as they spread, and some star spots will become submerged in the noise, resulting in decreased accuracy in centroid extraction and attitude estimation, and in some cases, identification failure. To enhance the dynamic performance of star sensors, Ma et al. (2025) recommend restoring these star streaks.

Blind and non-blind restoration algorithms for star image restoration algorithms can be categorized according to whether external angular velocity or angular acceleration information can be obtained. In addition, with the rapid development of neural networks, an increasing number of deep learning-based image restoration algorithms have been proposed. However, there is still a significant gap between these

‡ Corresponding author
ORCID: Yang LIU, https://orcid.org/0009-0008-9253-2683
© Zhejiang University Press 2025

methods and their practical deployment in star sensor systems (Wang et al. (2020).)

Blind restoration algorithms estimate blur parameters exclusively from a single-frame star image without angular velocity information (Sun et al. (2013); Jiang et al. (2017); ?); Yang et al. (2025)). Although these approaches are convenient and straightforward to implement, their estimation accuracy is significantly lower than non-blind restoration methods.

In the non-blind methods, the blur kernel can be obtained by angular velocity and acceleration using external devices (Sun et al. (2014b); Wang et al. (2014); Fei et al. (2012); Wang et al. (2018)). However, these algorithms have dual limitations. First, they overlook the error caused by gyro drift, disregarding its impact on the overall accuracy of the restoration process. Sun et al. used the extended Kalman filter (EKF) to estimate the position of individual star spots and gyro drift under dynamic conditions (Sun et al. (2014a)). However, their method suffers from increasing computational redundancy as the number of star points increases, because each star must be processed separately. Second, these methods rely on preliminary angular velocity assumptions, estimating the star spot's trailing path based on prior angular velocity, and interpreting motion blur in star images in a linear manner to calculate the blur kernel. For example, Yi et al. (2023) assume that the angular velocity is perpendicular to the Z-axis of the star sensor, so the star spots form straight lines on the image plane, and then the linear blur kernels are calculated according to the trajectories. Ma et al. (2016) established a proportional relationship between the rotation angle perpendicular to the Z-axis and the field of view. This relationship is used to estimate the linear blur kernel. Zhang et al. (2012) hypothesized that the star sensor undergoes rotation around the Z-axis, resulting in star spots forming arcs on the image plane. Then the blur kernel is calculated according to the corresponding chord. However, these priors and linear explanation cannot fully capture the non-uniform and nonlinear nature of the motion blur present in star images (Spiller and Curti (2022)). Therefore, addressing these shortcomings is crucial for enhancing the robustness and precision of the star image restoration algorithm.

Inspired by the study by Sun et al., we proposes a multiplication extended Kalman filter (MEKF)-aided non-blind star image restoration algorithm based on a heterogeneous blur kernel to address the two aforementioned challenges, assuming a one-to-one correspondence between the spacecraft attitude and the star spot positions on the image plane. MEKF is one of the most widely used attitude estimation methods in the aerospace field (Lefferts et al. (1982); Markley (2003); Sola (2017); Tian et al. (2025)). MEKF has the advantage of not only suppressing gyro drift error, but also allowing its predicted attitude to be used to determine star spots regions, providing the initial conditions for the subsequent heterogeneous blur kernel estimation. To address non-uniform and non-linear motion blur in star images, the proposed algorithm emphasizes eliminating pixel-by-pixel motion blur is the key to image restoration. Therefore, a heterogeneous blur kernel is presented. In this algorithm, the traditional blur kernel is replaced by a set of diverse blur kernels, each tailored to the characteristics of a single pixel within the star regions. The pixel blur kernel is determined using its specific position and motion, which means that the calculation of the blur kernel no longer requires estimating the star spot's trailing path based on a priori angular velocity. This allows the algorithm to focus on understanding the root cause of the blur rather than relying solely on the image content. Such an innovative strategy enhances the adaptability of the restoration process and can more accurately deal with the complex motion blur existing in star images, making it suitable for image restoration in various situations.

The arrangement is as follows: The method of estimating gyro drift by MEKF is described in Section 2. Section 3 introduces The heterogeneous blur kernel estimation and regional star image restoration. Section 4 demonstrates the proposed algorithm's effectiveness through experiments and results. The conclusions are presented in Section 5.

2 State optimization estimation based on MEKF

After years of development, MEKF not only has a sound theory, but it has also been verified by several rigorous experiments, and thus plays an important role in attitude estimation. At present, it is widely used in the fields of robotics, navigation and sensor fusion. There are various kinds of attitude expres-

Unedited

sions, the quaternion being the most common due to its non-singularity and low dimension. However, although the quaternion has four terms, the quaternion only has three real degrees of freedom; one of these terms is limited by the other three terms and the norm of the quaternion. It signifies that the covariance matrix of the quaternion is theoretically singular, making some difficulties for numerical calculations. To solve this problem, modified Rodrigues parameters(MRP) a is used to describe attitude in this paper.

$$\frac{1}{4}\boldsymbol{a}=\frac{\underline{\boldsymbol{q}}}{1+q_4}=\boldsymbol{e}tan(\frac{\theta}{4}) \tag{1}$$

where $\boldsymbol{q}=\begin{bmatrix}\underline{\boldsymbol{q}}\\ q_4\end{bmatrix}=[q_1\ q_2\ q_3\ q_4]^T$ denotes the attitude quaternion, $\underline{\boldsymbol{q}}$ and q_4 denote the vector and scalar parts of the quaternion, respectively. $\boldsymbol{e}$ and θ represent the corresponding rotation axis and angle of the quaternion respectively. The coefficient term is to ensure that $a\approx\theta$ for small rotations.

As shown in Eq. (1), MRP is an unconstrained three-dimensional vector with the same number of parameters as degrees of freedom, avoiding the problem of over-parameterization. The singularities occur at $\theta=\pm 2\pi$, while MEKF always operates close to the origin. Thus, singularity is no longer a problem (Madyastha et al. (2011); Zamani et al. (2015)).

Before proceeding with the derivation of the subsequent content, Table 1 describes some of the variables used in this paper.

Table 1 Definitions of some variables.

Variables	Descriptions
$\boldsymbol{\omega}$	True value
$\tilde{\boldsymbol{\omega}}$	Estimated value
$\hat{\boldsymbol{\omega}}$	Measured value

2.1 Prediction

Attitude error MRP $\delta\boldsymbol{a}$ and gyro drift $\boldsymbol{b}$ are selected as state vectors x.

$$\boldsymbol{x}=[\delta\boldsymbol{a}\ \boldsymbol{b}]^T \tag{2}$$

A widely used model of the gyro is given as follows

$$\begin{aligned}\boldsymbol{\omega}&=A_{bg}(\boldsymbol{\omega}_g-\boldsymbol{b}-\boldsymbol{\eta}_g)\\ \dot{\boldsymbol{b}}&=\boldsymbol{\eta}_r\end{aligned} \tag{3}$$

where $\boldsymbol{\omega}$ and $\boldsymbol{\omega}_g$ denote the true and measured angular velocity respectively. $\boldsymbol{\eta}_g$ and $\boldsymbol{\eta}_r$ denote zero-mean Gaussian white noises. To facilitate the subsequent derivation, the gyro coordinate system is assumed to be consistent with the body coordinate system of the satellite, that is, $A_{bg}=I_{3*3}$.

The estimated gyro angular velocity $\tilde{\boldsymbol{\omega}}_g$ is described as

$$\tilde{\boldsymbol{\omega}}_g=\boldsymbol{\omega}_g-\tilde{\boldsymbol{b}} \tag{4}$$

where $\tilde{\boldsymbol{b}}$ denotes the estimated drift of the gyro.

Letting $\otimes$ denotes the multiplication of quaternions, the error quaternion and quaternion differential equation are shown in Eqs (5) and (6), respectively.

$$\tilde{\boldsymbol{q}}=\boldsymbol{q}\otimes\delta\boldsymbol{q} \tag{5}$$

$$\dot{\boldsymbol{q}}=\frac{1}{2}\boldsymbol{q}\otimes\begin{bmatrix}\boldsymbol{\omega}\\ 0\end{bmatrix} \tag{6}$$

where $\tilde{\boldsymbol{q}}$ and $\boldsymbol{q}$ denote the estimated and true quaternions, respectively. $\delta\boldsymbol{q}$ denotes the error quaternion which can be obtained by integrating the angular velocity.

Differentiate both sides of Eqs (5) and (6) so that it can obtain

$$\dot{\delta\boldsymbol{q}}=\frac{1}{2}\delta\boldsymbol{q}\otimes\begin{bmatrix}\tilde{\boldsymbol{\omega}}\\ 0\end{bmatrix}-\frac{1}{2}\begin{bmatrix}\boldsymbol{\omega}\\ 0\end{bmatrix}\otimes\delta\boldsymbol{q} \tag{7}$$

Then, Eqs (1) and (7) are combined to obtain the partial derivative of δa with respect to time.

$$\dot{\delta\boldsymbol{a}}=((1-\frac{\delta\boldsymbol{a}^T\delta\boldsymbol{a}}{16})I_{3\times3}+\frac{\delta\boldsymbol{a}\delta\boldsymbol{a}^T}{8})(\tilde{\boldsymbol{\omega}}-\boldsymbol{\omega})-\frac{1}{2}[(\tilde{\boldsymbol{\omega}}+\boldsymbol{\omega})\times]\delta\boldsymbol{a} \tag{8}$$

where $[\boldsymbol{\omega}\times]$ is the following matrix.

$$[\boldsymbol{\omega}\times]=\begin{bmatrix}0&-\omega_z&\omega_y\\ \omega_z&0&-\omega_x\\ -\omega_y&\omega_x&0\end{bmatrix} \tag{9}$$

The state transition equations can be described as

$$\dot{\boldsymbol{x}}(t)=f(\boldsymbol{x}(t))+\boldsymbol{w}(t) \tag{10}$$

$\boldsymbol{w}(t)$ denotes the process noise which is assumed to be zero-mean Gaussian noise with covariance Q.

The expression of the state transition equation in the discrete case is as follows.

$$\begin{aligned}\tilde{\boldsymbol{x}}_{k+1}^{-}&=\tilde{\boldsymbol{x}}_k^{+}+\frac{\partial\boldsymbol{x}}{\partial t}|_{\boldsymbol{x}=\tilde{\boldsymbol{x}}_k^{+}}\delta t+\frac{1}{2}\frac{\partial^2\boldsymbol{x}}{\partial t^2}|_{\boldsymbol{x}=\tilde{\boldsymbol{x}}_k^{+}}\delta t^2\\ &=\tilde{\boldsymbol{x}}_k^{+}+\boldsymbol{f}_k\delta t+\frac{1}{2}A_k\boldsymbol{f}_k\delta t^2\end{aligned} \tag{11}$$

Unedited

where $\tilde{\boldsymbol{x}}_k^+$ is

$$\tilde{\boldsymbol{x}}_k^+ = \begin{bmatrix} \tilde{\delta \boldsymbol{a}_k} \\ \tilde{\boldsymbol{b}}_k^+ \end{bmatrix} \tag{12}$$

The attitude error $\tilde{\delta \boldsymbol{a}_k}$ between step k and $k+1$ can be approximated by multiplying the attitude error of the gyro sampling interval.

$$q(\tilde{\delta \boldsymbol{a}_k}) = \delta \boldsymbol{q}_{g,1} \otimes ... \otimes \delta \boldsymbol{q}_{g,n} \tag{13}$$

where $\delta \boldsymbol{q}_{g,i}$ is the error quaternions between gyro sampling intervals between steps k and $k+1$.

$$\delta \boldsymbol{q}_g = \begin{bmatrix} \frac{1}{2}\tilde{\boldsymbol{\omega}}_g \delta t_g \\ 1 \end{bmatrix} \tag{14}$$

$\boldsymbol{f}_k$ can be obtained from Eqs (3) and (8).

$$\boldsymbol{f}_k = \frac{\partial \boldsymbol{x}}{\partial t}|_{\boldsymbol{x}=\tilde{\boldsymbol{x}}_k^+} = \begin{bmatrix} \dot{\delta \boldsymbol{a}} \\ \dot{\boldsymbol{b}} \end{bmatrix} \tag{15}$$

A_k is a Jacobian matrix.

$$\begin{aligned} A_k = \frac{\partial \boldsymbol{f}}{\partial \boldsymbol{x}}|_{\boldsymbol{x}=\tilde{\boldsymbol{x}}_k^+} &= \begin{bmatrix} \frac{\partial \dot{\delta \boldsymbol{a}}}{\partial \delta \boldsymbol{a}} & \frac{\partial \dot{\delta \boldsymbol{a}}}{\partial \boldsymbol{b}} \\ \frac{\partial \boldsymbol{\eta}_r}{\partial \delta \boldsymbol{a}} & \frac{\partial \boldsymbol{\eta}_r}{\partial \boldsymbol{b}} \end{bmatrix} |_{\boldsymbol{x}=\tilde{\boldsymbol{x}}_k^+} \\ &= \begin{bmatrix} F_a & F_b \\ 0_{3\times 3} & 0_{3\times 3} \end{bmatrix} \end{aligned} \tag{16}$$

where F_a and F_b are

$$\begin{aligned} F_a =& \frac{1}{8}(\delta \boldsymbol{a}^T \delta \boldsymbol{\omega} \cdot I_{3\times 3} + \delta \boldsymbol{a} \delta \boldsymbol{\omega}^T - \delta \boldsymbol{\omega} \delta \boldsymbol{a}^T) \\ & - \frac{1}{2}[(\tilde{\boldsymbol{\omega}} + \boldsymbol{\omega})\times] \end{aligned} \tag{17}$$

$$F_b = ((1 - \frac{\delta \boldsymbol{a}^T \delta \boldsymbol{a}}{16})I_{3\times 3} + \frac{\delta \boldsymbol{a} \delta \boldsymbol{a}^T}{8}) - \frac{1}{2}[\delta \boldsymbol{a}\times] \tag{18}$$

$\delta \boldsymbol{\omega}$ can be calculated from Eqs (3) and (4).

$$\delta \boldsymbol{\omega} = \tilde{\boldsymbol{\omega}} - \boldsymbol{\omega} = \boldsymbol{b} - \tilde{\boldsymbol{b}} + \boldsymbol{\eta}_g \tag{19}$$

The predicted error covariance matrix P satisfies Eq. (20).

$$P_{k+1}^- = \phi_k P_k^+ \phi_k^T + G_k Q_k G_k^T \tag{20}$$

where ϕ_k is

$$\phi_k = I_{6\times 6} + A_k * \delta t \tag{21}$$

G_k is calculated by

$$G_k = \begin{bmatrix} \frac{\partial \dot{\delta \boldsymbol{a}}}{\partial \boldsymbol{\eta}_g} & \frac{\partial \dot{\delta \boldsymbol{a}}}{\partial \boldsymbol{\eta}_r} \\ \frac{\partial \boldsymbol{\eta}_r}{\partial \boldsymbol{\eta}_g} & \frac{\partial \boldsymbol{\eta}_r}{\partial \boldsymbol{\eta}_r} \end{bmatrix} = \begin{bmatrix} F_b & 0_{3\times 3} \\ 0_{3\times 3} & I_{3\times 3} \end{bmatrix} \tag{22}$$

and Q can be obtained by

$$Q_k = E[\begin{bmatrix} \boldsymbol{\eta}_g \\ \boldsymbol{\eta}_r \end{bmatrix} \begin{bmatrix} \boldsymbol{\eta}_g \\ \boldsymbol{\eta}_r \end{bmatrix}^T] \tag{23}$$

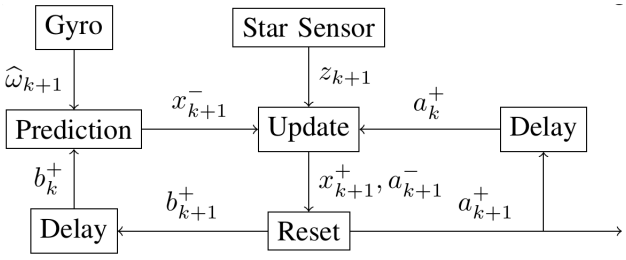

Fig. 1 Flow of the MEKF. MEKF, multiplication extended Kalman filter.

2.2 Improved update

The attitude z measured by the star sensor is used as the measurement vector and the attitude measurement equation is

$$\boldsymbol{z}(t) = q(\boldsymbol{a}(t)) \otimes q(\delta \boldsymbol{a}(t)) \tag{24}$$

where $\boldsymbol{a}(t)$ denotes the true attitude and $\delta \boldsymbol{a}(t)$ denotes zero-mean Gaussian measurement error with variance R.

The state vector is updated as follows

$$\begin{aligned} H_{k+1} &= [I_{3*3}\ 0_{3*3}] \\ S_{k+1} &= H_{k+1} P_{k+1}^- H_{k+1}^T + R_{k+1} \\ K_{k+1} &= P_{k+1}^- H_{k+1}^T S_{k+1}^{-1} \end{aligned} \tag{25}$$

$$\delta \boldsymbol{x}_{k+1}^+ = \begin{bmatrix} \delta \boldsymbol{a}_{k+1}^+ \\ \delta \boldsymbol{b}_{k+1}^+ \end{bmatrix} = K_{k+1}(q^{-1}(\tilde{\boldsymbol{a}}_{k+1}^-) \otimes \boldsymbol{z}_{k+1}) \tag{26}$$

$$P_{k+1}^{pred} = (I_{6\times 6} - K_{k+1} H_{k+1}) P_{k+1}^- \tag{27}$$

where $\tilde{\boldsymbol{a}}_{k+1}^-$ denotes the prediction attitude.

$$q(\tilde{\boldsymbol{a}}_{k+1}^-) = q(\tilde{\boldsymbol{a}}_k^+) \otimes q(\tilde{\delta \boldsymbol{a}}_{k+1}^-) \tag{28}$$

The updated state error is transferred to the attitude and reset to Eq. (29).

$$\begin{aligned} q(\tilde{\boldsymbol{a}}_{k+1}^+) &= q(\tilde{\boldsymbol{a}}_{k+1}^-) \otimes q(\delta \boldsymbol{a}_{k+1}^+) \\ \tilde{\boldsymbol{b}}_{k+1}^+ &= \tilde{\boldsymbol{b}}_{k+1}^- + \delta \boldsymbol{b}_{k+1}^+ \\ P_{k+1}^+ &= J_{k+1} P_{k+1}^{pred} J_{k+1}^T \end{aligned} \tag{29}$$

where J_{k+1} is

$$J_{k+1} = I_{3*3} - \frac{1}{2}[\delta \boldsymbol{a}_{k+1}^+ \times] \tag{30}$$

The detailed flow of the proposed MEKF is shown in Fig. 1.

Unedited

Table 2 Parameters of the star sensor.

Parameters	Unit	Typical value
Entrance pupil diameter	mm	25
Focal length	mm	25
Limiting magnitude		6
Exposure time	ms	80
Resolution	pixels	1024*1280
Pixel size	μm	5.3
Field of view	deg	12.5

3 Star image restoration

Table 2 lists some key parameters of the star sensor used in this paper. Subsequent discussions are based on these parameters.

As mentioned above, in the case of motion, the smearing effect reduces the accuracy of centroid extraction, resulting in decreased identification accuracy and success rates. Therefore, the motion-blurred image should be restored to improve the accuracy of centroid extraction.

3.1 Heterogeneous motion blur model

It is well known that the angular velocity of a star sensor typically possesses three-axis components. Furthermore, the trajectory of a star spot on the image plane is a segment of a conic curve, indicating that the motion blur in the star image is both non-uniform and nonlinear. If uniform or linear blur kernel is still used for star image restoration, the efficacy of the restoration process is compromised, resulting in reduced accuracy in centroid extraction. Therefore, a heterogeneous motion blur model is established to deal with non-uniform and nonlinear-blurred image restoration, in which the cause of motion blur of each pixel is considered rather than the content of the star image.

Letting $*$ as the general convolution operator, the image degradation model can be expressed as

$$g = h * f + \eta \tag{31}$$

where g and f denote the images before and after degradation respectively. h denotes the heterogeneous blur kernel map, with a different blur kernel for each pixel in f. η denotes the additive noise. Regardless of the additive noise, at each pixel of g, there is

$$g(i,j) = \sum_{i',j'} h_{i',j'}(i,j) f(i+i', j+j') \tag{32}$$

where $h_{i',j'}(i,j)$ denotes the blur kernel that operates on the pixel $(i+i', j+j')$ around the pixel (i,j).

The blur kernel estimation is the most important aspect of image restoration. According to Eq. (32), the heterogeneous blur kernel consists of a series of blur kernels, that are related to the position and motion of pixels (Gong et al. (2017)). As shown in Fig. 2, the motion of a pixel P located at (i,j) during the imaging process can be represented by a linear two-dimensional motion vector (u_P, v_P), where u_P and v_P represent the motion in the X-axis and Y-axis directions, respectively. Letting (x_0, y_0) as the intersection point of the main optical axis and the image plane of the star sensor, and f as the focal length, the two-dimensional motion vector (u_P, v_P) corresponding to pixel P can be expressed as

$$\begin{aligned} u_P &= (-\bar{\omega}_z(j-y_0) - \bar{\omega}_y f)\delta t \\ v_P &= (\bar{\omega}_z(i-x_0) + \bar{\omega}_x f)\delta t \end{aligned} \tag{33}$$

where $\bar{\boldsymbol{\omega}} = [\bar{\omega}_x \ \bar{\omega}_y \ \bar{\omega}_z]^T$ is the average angular velocity after compensating for the drift over the exposure time δt.

Then the blur kernel on P is expressed as

$$h_{i',j'}(P) = \begin{cases} 0, ||(i',j')||_2 \geq \dfrac{||\boldsymbol{m}_P||_2}{2} \\ \dfrac{1}{||\boldsymbol{m}_P||_2}\delta(u_P j' - v_P i'), otherwise \end{cases} \tag{34}$$

$$||\boldsymbol{m}_P||_2 = ||(u_P, v_P)||_2 \tag{35}$$

Although the proposed algorithm assumes that the blur kernel on a single pixel is linear, it makes no assumptions about the motion blur of the image, making the method suitable for various scenes and able to deal with various motion blurs.

3.2 Estimation of Star Region and Blur Kernel

With MEKF the predicted attitude q can be obtained. Assuming that the coordinate system of the star sensor is aligned with that of the satellite, and the main optical axis of the star sensor under the satellite coordinate system is denoted as Z_0, then the

Unedited

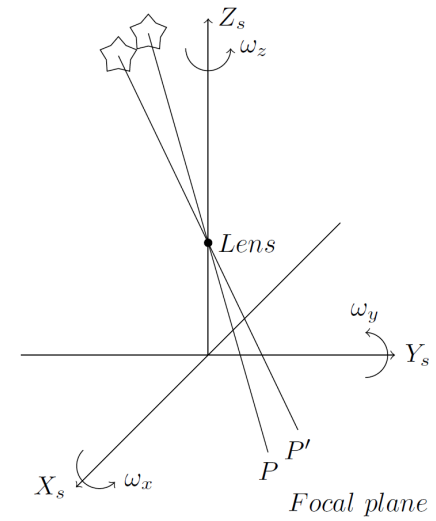

(a)Imaging model of star sensor.

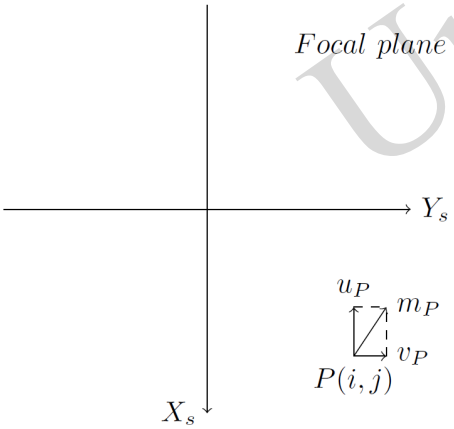

(b)Blur kernel on a single pixel.

Fig. 2 Position and blur kernel of the star spot.

optical axis direction Z under the inertial frame can be calculated by Eq. (36).

$$\begin{bmatrix} \boldsymbol{Z} \\ 0 \end{bmatrix} = \boldsymbol{q} \otimes \begin{bmatrix} \boldsymbol{Z}_0 \\ 0 \end{bmatrix} \otimes \boldsymbol{q}^{-1} \tag{36}$$

The angle between the star vector in the navigation star catalog and the optical axis in the inertial frame is calculated. Star vectors with angles less than half the field of view are converted to the sensor coordinate system and projected onto the image plane. The projection positions correspond to the star positions at the center of the exposure time.

Assuming the vector of the star spot in the field of view is v under the reference frame and w under the sensor frame, and the attitude quaternion is q, the vector transformations can be expressed as Eq. (37).

$$\begin{bmatrix} \boldsymbol{w} \\ 0 \end{bmatrix} = \boldsymbol{q}^{-1} \otimes \begin{bmatrix} \boldsymbol{v} \\ 0 \end{bmatrix} \otimes \boldsymbol{q} = \frac{[x - x_0 \; y - y_0 \; -f]^T}{\sqrt{(x-x_0)^2 + (y-y_0)^2 + f^2}} \tag{37}$$

where (x_0, y_0) is the intersection of the main optical axis and the image plane, f is the focal length of the star sensor and (x, y) is the center of the star's projection on the image plane. These parameters are measured in pixels to reduce the complexity of the calculation.

The update rate of the gyro is usually hundreds of Hertz, therefore the angular velocity is considered as a constant between the adjacent sampling intervals of the gyro, and the corresponding error quaternion $\delta \boldsymbol{q}_t^{t+\delta t}$ can be calculated according to Eq. (14).

By combining Eqs (14) and (37), the estimation of the star vector $w_{t+\delta t}$ at time $t+\delta t$ can be obtained.

$$\begin{bmatrix} \boldsymbol{w}_{t+\delta t} \\ 0 \end{bmatrix} = (\delta \boldsymbol{q}_t^{t+\delta t})^{-1} \otimes \begin{bmatrix} \boldsymbol{w}_t \\ 0 \end{bmatrix} \otimes \delta \boldsymbol{q}_t^{t+\delta t} \tag{38}$$

The star position at time $t + \delta t$ can be obtained by

$$\begin{cases} x_{t+\delta t} = -\dfrac{w_{t+\delta t,x}}{w_{t+\delta t,z}} f + x_0 \\ y_{t+\delta t} = -\dfrac{w_{t+\delta t,y}}{w_{t+\delta t,z}} f + y_0 \end{cases} \tag{39}$$

Similarly, the star position at time $t - \delta t$ can also be derived. Then the star position (x_i, y_i) corresponding to each gyro sampling during the entire exposure time is obtained. According to these positions, the motion trajectory of the star spot on the image plane can be obtained, and the region within

Unedited

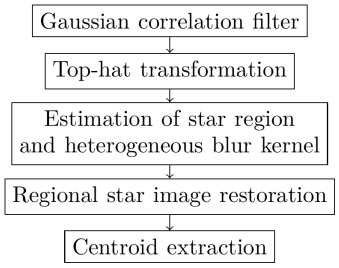

Fig. 3 Flow of dynamic star image restoration.

four pixels of the trajectory is taken as the star region. The heterogeneous blur kernel of the star region is calculated by Eqs (33) and (34).

3.3 Regional Image Restoration

As seen from Eq. (31), even if the blur kernel is obtained, the presence of additive noise makes it difficult to obtain a deblurred image by deconvolution. At present, the pre-processing of dynamic star images is relatively mature, and Gaussian correlation filter and top-hat transformation are used for denoising (Sun et al. (2013)Bright and Steel (1987)). Next, the process of regional image restoration is introduced.

To accelerate the algorithm, image restoration is performed only in the star region. According to Bayes' theorem and Eq. (32), image restoration that eliminates image noise can be expressed as an iterative process.

$$\begin{aligned} f^{r+1}(i) &= f^r(i) \sum_k \frac{h_i(k) g(k)}{\sum_j h_j(k) f^r(j)} \\ f^1(i) &= \sum_k \frac{h_i(k) g(k)}{\sum_j h_j(k)} \end{aligned} \tag{40}$$

where r represents the number of iterations, and i, j, and k represent the index of pixels.

The whole process of star image restoration is introduced on this basis, as shown in Fig. 3.

4 Simulations and results

To confirm the effectiveness of the proposed algorithm, a mathematical simulation model with adjustable parameters is established based on Simulink and a micro-satellite orbiting at an altitude of 490km. The model is shown in the Fig. 4. In the simulation experiment, the input of the model is the initial attitude, angular velocity and orbit time, and

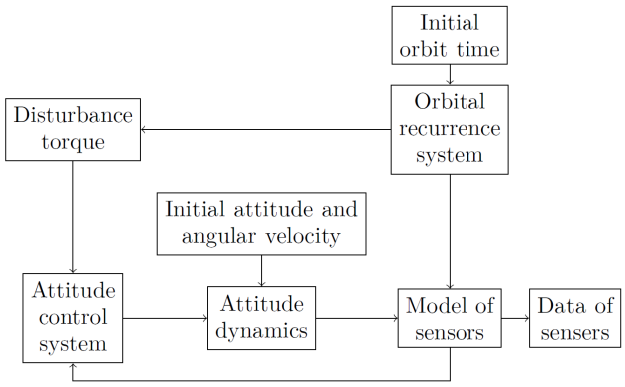

Fig. 4 Simulation model.

the output is the real attitude determined by the attitude dynamics module and sensor measurement data. The update rates of the star sensor and the gyro of the micro-satellite are 5Hz and 100Hz, respectively. The simulation experiments are divided into following parts:

1. Estimation of the star region and blur kernel is closely related to MEKF performance. Therefore, the attitude and gyro drift estimation accuracy of the MEKF are tested under different angular velocities.

2. To validate the restoration performance of the algorithm on non-linear motion-blurred images of varying degrees, the performance of the proposed algorithm is compared with that of two other linear blur kernel estimation algorithms on the nonlinear-blurred star images with different proportions of Z-axis components of angular velocities.

3. To assess the suitability and effectiveness of the proposed algorithm, the restoration effects of the proposed algorithm and the other two algorithms on blurred images with different angular velocities are compared. In addition, the proposed algorithm with uncompensated measurement error of the star sensor and gyro drift is also used as a comparison to evaluate the improvement of MEKF in image restoration. Furthermore, the attitude estimation accuracy of the star image recovered by the proposed algorithm is tested.

The simulated motion-blurred star image is generated as follows (Li et al. (2013)): First, a preset angular velocity is input into the attitude dynamics

Unedited

Fig. 5 Simulated motion-blurred star image.

module of the satellite simulation model to generate the corresponding attitude, the measured angular velocity and the measured attitude quaternion. The measurement errors are shown in Table 3. Measurements from the gyro and star sensor are used for MEKF to estimate drift and attitude. Second, a series of continuous simulated static star images is generated according to the unbiased attitude, and then the static star images are blurred according to the preset angular velocity during the exposure time. Finally, the simulated motion-blurred star images are obtained by adding Gaussian noise. One of the simulated motion-blurred star images is shown in Fig. 5.

4.1 The performance of MEKF

In the simulation, the inertial frame is selected as the reference frame and the initial attitude quaternion of the satellite is $[0\ 0\ 0\ 1]^T$. The measurement models of the star sensor and gyro are Eqs (5) and (3) respectively. The fixed noise is shown in Table 3, where ARW and RRW represent angle random walk and rate random walk, respectively. The angular velocity is set in an arbitary direction, increasing from 5deg/s to 10deg/s with a step size of 0.1deg/s. The index of attitude estimation accuracy is the root mean square error (RMSE) of the three-axis error angle after convergence of MEKF, and the error angle is given by 1. The index of gyro drift estimation accuracy is the RMSE of the difference between the estimated value and the true value after the convergence of MEKF.

Table 3 Fixed noise.

Variable		Unit	Value
$\delta\boldsymbol{\theta}$	x	arcsec	30
	y		30
	z		200
$\boldsymbol{b}$	x	deg/s	0.2
	y		0.5
	z		0.1
ARW		$\mathrm{deg}/\sqrt{\mathrm{hr}}$	0.15
RRW		$\mathrm{deg/hr}/\sqrt{\mathrm{hr}}$	1

Fig. 6 shows the estimation errors of attitude and gyro drift at an angular velocity of 5deg/s, and Fig. 7 shows the details of the estimation errors for attitude and gyro drift after the MEKF convergence between 200s and 1000s. It can be seen that MEKF converges quickly and can effectively suppress the measurement error of the star sensor and accurately estimate the gyro drift. The estimation accuracy of attitude and gyro drift is shown in Fig. 8. The three-axis estimation accuracy of attitude and gyro drift is about $[22.38\ \ 22.31\ \ 68.42]^T$ arcsec and $[2.618{*}10^{-3}\ \ 2.6612{*}10^{-3}\ \ 2.577{*}10^{-3}]^T$ deg/s, respectively, providing favorable initial conditions for the subsequent estimation of star region and blur kernel.

4.2 The restoration effect of a nonlinear-blurred image with different degrees

The attitude and gyro drift estimated by MEKF are used to calculate the heterogeneous blur kernel and other two blur kernels respectively. The calculation of the blur kernels (l, θ) proposed by Yi et al. (2023) and Ma et al. (2016) is as Eqs (41) and (42), respectively.

$$\begin{aligned} l &= \sum_{m=1}^{n} \sqrt{(x_i^m - x_i^{m-1})^2 + (y_i^m - y_i^{m-1})^2} \\ \theta &= \frac{1}{n} \sum_{m=1}^{n} arctan(\frac{y_i^{t+m\delta t} - y_i^{t+(m-1)\delta t}}{x_i^{t+m\delta t} - x_i^{t+(m-1)\delta t}}) \end{aligned} \tag{41}$$

$$\begin{aligned} l &= \left\lfloor \frac{\sqrt{\omega_x^2 + \omega_y^2} \cdot T}{\theta_{FOV}} \cdot N \right\rfloor \\ \theta &= arctan(\frac{\omega_x}{\omega_y}) \end{aligned} \tag{42}$$

where (x_i^m, y_i^m) represents the position of the i-th star at the m time of gyro sampling within the

Unedited

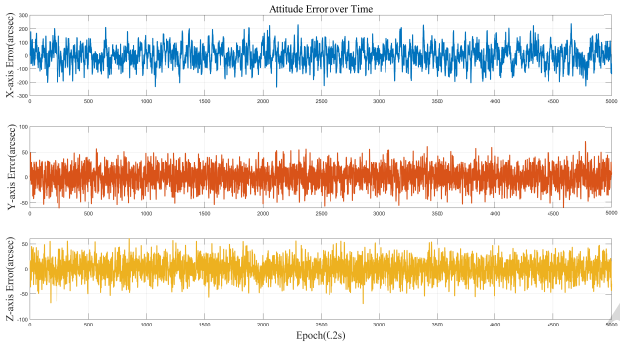

(a)Error angle.

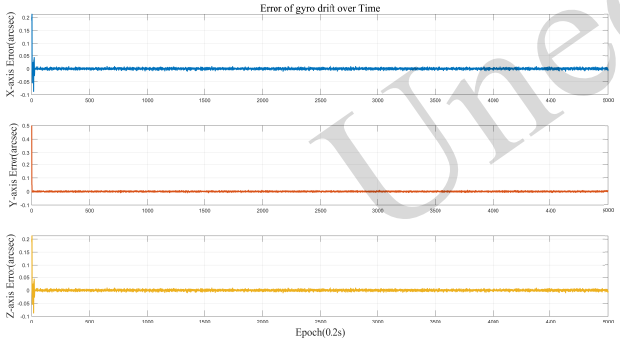

(b)Error of gyro drift.

Fig. 6 Performance of MEKF at an angular velocity of 5 deg/s. MEKF, multiplication extended Kalman filter.

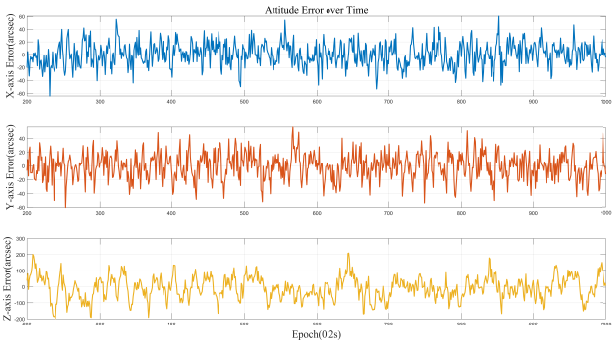

(a)Error angle.

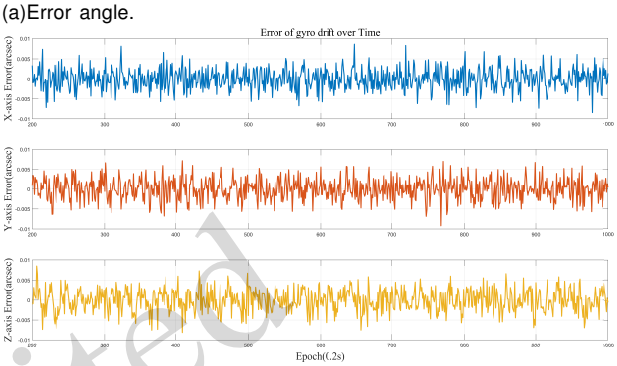

(b)Error of gyro drift.

Fig. 7 Performance details of MEKF at an angular velocity of 5 deg/s. MEKF, multiplication extended Kalman filter.

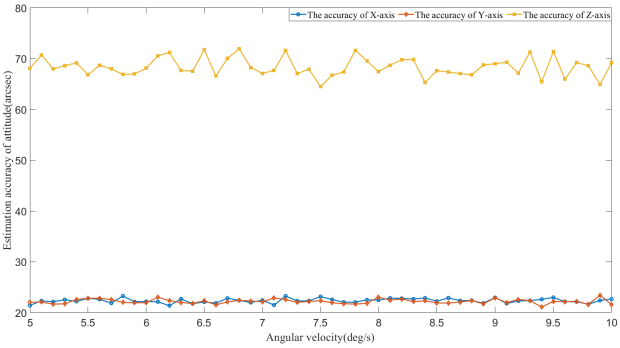

(a)Estimation accuracy of attitude.

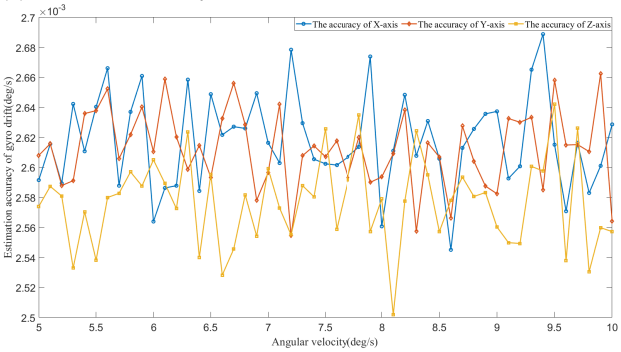

(b)Estimation accuracy of gyro drift.

Fig. 8 Global performance of MEKF. MEKF, multiplication extended Kalman filter.

Unedited

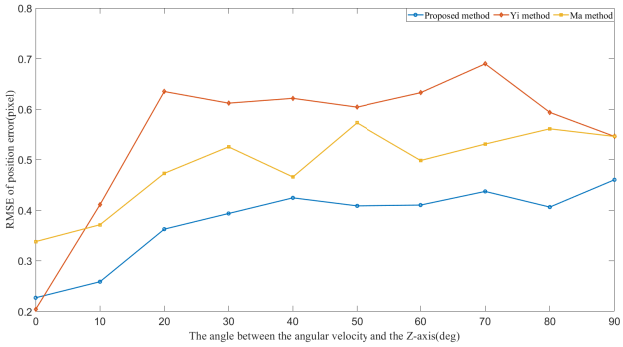

Fig. 9 RMSE of position error when σ is 5. RMSE, root mean square error.

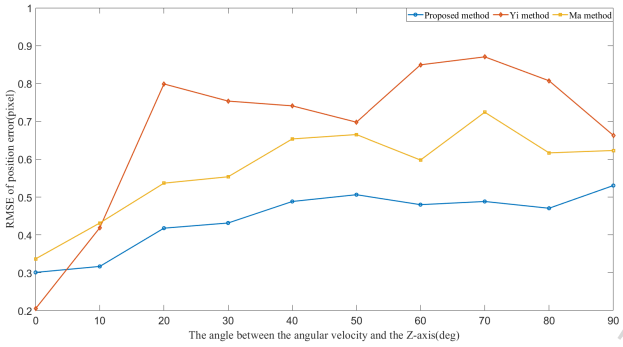

Fig. 10 RMSE of position error when σ is 7. RMSE, root mean square error.

exposure time. n denotes the total number of times the gyro collects data within one exposure time of the star sensor. The compensated angular velocity is denoted by $\boldsymbol{\omega} = (\omega_x\ \omega_y\ \omega_z)^T$, where T and θ_{FOV} denote the exposure time and field of view of the star sensor, respectively. N denotes the number of pixels corresponding to the field of view. $\lfloor\rfloor$ signifies the operation of rounding down to the nearest integer.

The star images with different degrees of nonlinear motion blur correspond to different proportions of the Z-axis components of angular velocity. In this simulation, the modulus of the angular velocity is fixed at 10deg/s. The angle between the angular velocity vector and the Z-axis is incremented from 0deg to 90deg with a step size of 10deg. For each set of angular velocity, simulated motion-blurred star images are generated, and Gaussian noises with a mean of 20 and a standard deviation σ of 5, 7, and 10 are added respectively. Then, the three algorithms are used for image restoration and centroid extraction, and the performances of the algorithms are evaluated by the RMSE of the position error of centroid extraction.

The image restoration results of the proposed algorithm are shown in Fig. 12. It is evident from Fig. 12 that the algorithm effectively concentrates

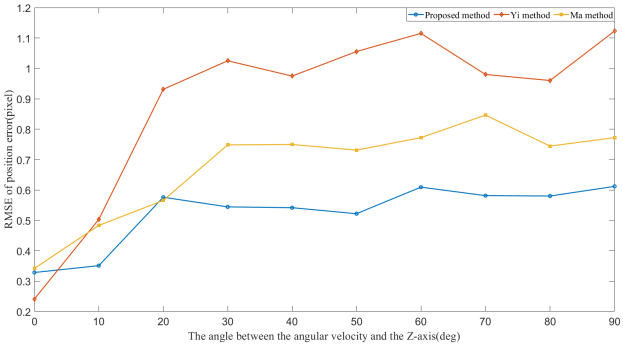

Fig. 11 RMSE of position error when σ is 10. RMSE, root mean square error.

the energy of dispersed star points.

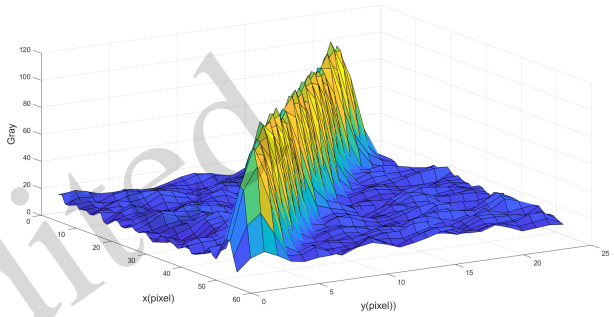

(a)Motion blurred star spot.

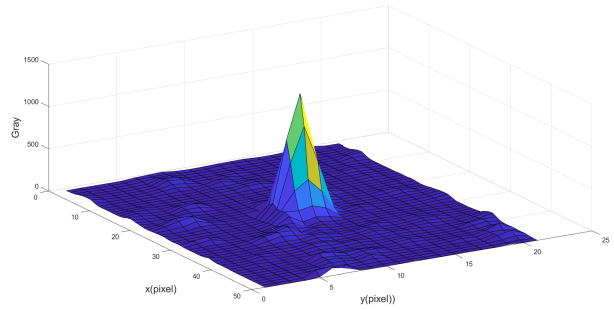

(b)Star spot recovered by the proposed algorithm.

Fig. 12 image restoration effect of the proposed algorithm.

The RMSE of position errors of three algorithms under different degrees of nonlinear motion blur and various noise conditions is shown in Figs 9-11. When the Z-axis component of the angular velocity is relatively high, the image restoration accuracy of each algorithm is higher. This is because although the angular velocity reaches 10deg/s, the trailing length at the edge of the image is about 7.15 pixels, while there is almost no trailing of the star spot near the center of the image. In this case, compared with the method proposed by Ma, which directly extracts

Unedited

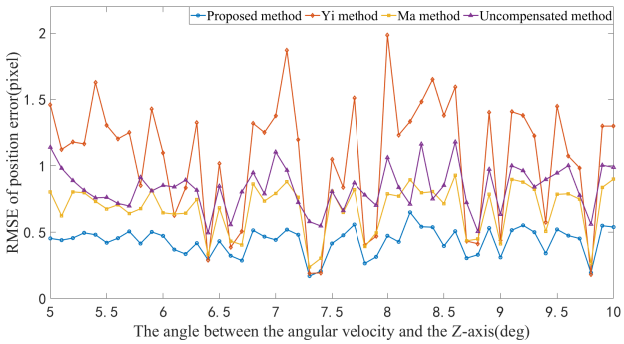

Fig. 13 RMSE of extraction accuracy with varying angular velocities. RMSE, root mean square error.

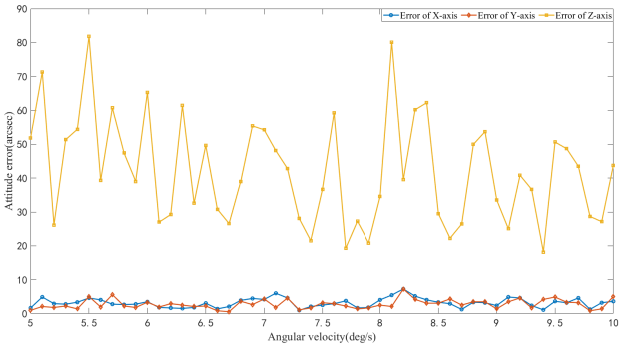

Fig. 14 Attitude estimation accuracy with varying angular velocities.

the centroids of star spots, the other two methods have higher accuracy. As the proportion of the Z-axis component of the angular velocity decreases, the extraction accuracies of the other two methods fluctuate greatly, while the proposed algorithm is more accurate and stable. In addition, compared with the other two methods, the proposed method demonstrates robustness to noise. With the increase of noise, even if the standard deviation σ of Gaussian noise reaches 10, the extraction accuracy can still be maintained at about 0.6 pixels.

4.3 Performance of image restoration

To evaluate the performance of the three methods, the angular velocity is varied within the range of 5deg/s to 10 deg/s with a step size of 0.1deg/s, and the direction of angular velocity is set to any direction. The simulated motion-blurred star images are generated based on each set of angular velocity, and Gaussian noise with a mean of 20 and a standard deviation σ of 5 is added. Furthermore, to verify the optimization effect of MEKF in removing measurement noise and gyro drift on image restoration, the heterogeneous blur kernel estimation algorithm with uncompensated error is also used for comparison. The four methods are used for star image restoration and centroid extraction, and the performances of the methods are evaluated by the RMSE of the accuracy of centroid extraction.

As shown in Fig. 13, using MEKF for the estimation and compensation of measurement errors from the star sensor and gyro drift leads to a significant enhancement in the accuracy of centroid extraction. In addition, since the proposed algorithm is pixel-by-pixel deblurring based on the cause of motion blur, the extraction accuracies of various motion-blurred star images are relatively stable, while the restoration effects of the other two algorithms fluctuate greatly with the change of angular velocity. The average values of the extraction accuracy and computation time are presented in Table 4. Compared with the uncompensated method, the star extraction accuracy of the proposed algorithm is improved by 48.11% after compensating for the measurement error of the star sensor and gyro drift with MEKF. Compared with the other two algorithms, the extraction accuracy of the proposed algorithm is improved by 59.64% and 36.63%, respectively. However, the proposed algorithm takes a long time for blur kernel estimation and image restoration, because the proposed algorithm needs to calculate the blur kernel corresponding to each pixel in the star region. If only the star region is restored, the required time is close to the time of restoring the whole star image with a single blur kernel, which is also the limitation of the entire algorithm.

Then the star spots recovered by the proposed method are utilized for attitude estimation, and the accuracy of attitude estimation is quantified as the RMSE of the three-axis error angle according to 1. The result is shown in Fig. 14.

Compared with the initial measurement noise $[30\ 30\ 200]^T$ arcsec of the star sensor, the proposed algorithm has an average attitude estimation accuracy of $[3.317\ 2.913\ 42.13]^T$ arcsec, the accuracy of the pointing axis is improved by 78.93%, and the accuracy of the other two axes is improved by 88.94% and 90.29%, which greatly improves the dynamic performance of the star sensor.

Unedited

Table 4 Performance of the algorithm

Methods	Extraction accuracy (pixel)	Time of blur kernel estimation(ms)	Time of restoration(ms)
Proposed method	0.4319	1.6	97.7
Ma method	1.07	$1.1*10^{-2}$	2.4
Yi method	0.6816	$6.9*10^{-3}$	104
Uncompensated method	0.8324	1.5	98.5

5 Conclusions

The MEKF-aided non-blind star image restoration algorithm based on the heterogeneous blur kernel is proposed to address challenges in estimating gyro drift and restoring non-uniform and nonlinear motion-blurred images. The simulation results indicate that the proposed algorithm can effectively eliminate the measurement error of the star sensor and the gyro drift and improve the effect of star image restoration. After compensating for the error, the performance of the proposed algorithm is improved by 48.11%. The proposed algorithm is also robust to image noise. Even if the standard deviation σ of Gaussian noise reaches 10, the extraction accuracy after image restoration with a heterogeneous blur kernel can still be maintained at about 0.6 pixels. Compared with the existing algorithms, when the proposed algorithm is used to estimate the heterogeneous blur kernel and restore the star image, the extraction accuracy is improved by 59.64% and 36.63%, respectively. Compared with the initial measurement noise, the accuracy of the pointing axis is improved by 78.93%, and the accuracy of the other two axes is improved by 88.94% and 90.29% respectively. Simulations reveal that the proposed algorithm exhibits high precision, is robust to noise, and is suitable for the restoration of various motion-blurred images.

Moreover, while the proposed algorithm demonstrates promising performance, it also presents certain limitations. First, the pixel-wise heterogeneous blur kernel estimation introduces high computational complexity, which may hinder real-time applications, especially in high-resolution scenarios. Second, the current evaluation is primarily based on simulated star images with an idealized noise model. Due to the limited availability of real star images under high dynamic conditions, actual star-sensitive data have not been used for validation. As a result, discrepancies between the simulated and real-world noise distributions may exist, potentially affecting the generalizability of the results. Future research will focus on reducing the algorithm's computational load—potentially via model simplification, parallel processing, or hardware acceleration—and validating the proposed method using real on-orbit data to further assess its robustness under practical conditions.

Unedited

References

Bright DS, Steel EB, 1987. Two-dimensional top hat filter for extracting spots and spheres from digital images. *Micros*, 146(2):191-200. https://doi.org/10.1111/j.1365-2818.1987.tb01340.x

Fei X, Nan C, Zheng Y, et al., 2012. A novel approach based on mems-gyro's data deep coupling for determining the centroid of star spot. *Math Probl Eng*, 2012(1):403584. https://doi.org/10.1155/2012/403584

Gong D, Yang J, Liu L, et al., 2017. From motion blur to motion flow: A deep learning solution for removing heterogeneous motion blur. Proc IEEE Conf on computer vision and pattern recognition, p.2319-2328, https://doi.org/10.1109/CVPR.2017.405

Jiang J, Huang J, Zhang G, 2017. An accelerated motion blurred star restoration based on single image. *IEEE Sens J*, 17(5):1306-1315. https://doi.org/10.1109/JSEN.2016.2645861

Lefferts EJ, Markley FL, Shuster MD, 1982. Kalman filtering for spacecraft attitude estimation. *J Guid, control, Dyn*, 5(5):417-429. https://doi.org/10.2514/3.56190

Li AJ, Liu CS, Shen Xf, 2013. An approach to star map simulation for star sensor considering the effect of image motion. *Opt Photonics J*, 3(2B):108-111. https://doi.org/10.4236/opj.2013.32B027

Ma L, Bernelli-Zazzera F, Jiang G, et al., 2016. Region-confined restoration method for motion-blurred star image of the star sensor under dynamic conditions. *Appl Opt*, 55(17):4621-4631. https://doi.org/10.1364/AO.55.004621

Ma L, Dai D, Ni Y, 2025. How to improve the attitude accuracy of the star sensor under dynamic conditions: A review. *Acta Astronaut*, 233:42-54. https://doi.org/10.1016/j.actaastro.2025.03.043

Madyastha V, Ravindra V, Mallikarjunan S, et al., 2011. Extended kalman filter vs. error state kalman filter for aircraft attitude estimation. Proc AIAA Guidance, Navigation, and Control Conf, p.article 6615, https://doi.org/10.2514/6.2011-6615

Markley FL, 2003. Attitude error representations for kalman filtering. *J guid control, dyn*, 26(2):311-317. https://doi.org/10.2514/2.5048

Sola J, 2017. Quaternion kinematics for the error-state kalman filter, . https://arxiv.org/abs/1711.02508

Spiller D, Curti F, 2022. A geometrical approach for the angular velocity determination using a star sensor. *Acta Astronaut*, 196:414-431. https://doi.org/10.1016/j.actaastro.2020.11.043

Sun T, Xing F, You Z, et al., 2013. Motion-blurred star acquisition method of the star tracker under high dynamic conditions. *Opt Express*, 21(17):20096-20110. https://doi.org/10.1364/OE.21.020096

Sun T, Xing F, You Z, et al., 2014a. Deep coupling of star tracker and mems-gyro data under highly dynamic and long exposure conditions. *Meas Sci and Technol*, 25(8):085003. https://doi.org/10.1088/0957-0233/25/8/085003

Sun T, Xing F, You Z, et al., 2014b. Smearing model and restoration of star image under conditions of variable angular velocity and long exposure time. *Opt express*, 22(5):6009-6024. https://doi.org/10.1364/OE.22.006009

Tian C, Hao N, He F, 2025. T-eskf: Transformed error-state kalman filter for consistent visual-inertial navigation. *IEEE robot autom lett*, 10(2):1808-1815. https://doi.org/10.1631/FITEE.1900590

Wang H, Wang Zy, Wang Bd, et al., 2020. An artificial intelligence enhanced star identification algorithm. *Front Inf Technol Electron Eng*, 21(11):1661-1670. https://doi.org/10.1631/FITEE.1900590

Wang K, Zhang C, Li Y, et al., 2014. A new restoration algorithm for the smeared image of a sins-aided star sensor. *J Navig*, 67(5):881-898. https://doi.org/10.1017/S0373463314000277

Wang S, Zhang S, Ning M, et al., 2018. Motion blurred star image restoration based on mems gyroscope aid and blur kernel correction. *Sensors*, 18(8):2662. https://doi.org/10.3390/s18082662

Yang L, Huajian D, Yuchen L, et al., 2025. Motion parameters estimation algorithm of star sensor based on zernike moments under dynamic conditions. *Meas Sci Technol*, 36(5):055104. https://doi.org/10.1088/1361-6501/adc1ec

Yi J, Ma Y, Zhu Z, et al., 2023. A blurred star image restoration method based on gyroscope data and enhanced sparse model. *Meas Sci and Technol*, 34(11):115105. https://doi.org/10.1088/1361-6501/ace730

Zamani M, Trumpf J, Mahony R, 2015. Nonlinear attitude filtering: A comparison study, . https://arxiv.org/abs/1502.03990

Zhang W, Quan W, Guo L, 2012. Blurred star image processing for star sensors under dynamic conditions. *Sensors*, 12(5):6712-6726. https://doi.org/10.3390/s120506712

Unedited